Higher-order topological superconductivity in monolayer WTe$_2$ from repulsive interactions

Ammar Jahin and Yuxuan Wang

Department of Physics, University of Florida, 2001 Museum Road, Gainesville, Florida 32611, USA

Superconductivity has been experimentally observed in monolayer WTe$_2$, in which the suggested in-plane field measurements are of a spin-triplet nature. Furthermore, it has been proposed that with a *p*-wave pairing, the material is a second-order topological superconductor with a pair of Majorana zero modes at the corners of a finite sample. We show that for a repulsive on-site interaction and sizable Fermi surfaces, the desired *p*-wave state arises naturally due to the Kohn-Luttinger mechanism, and indeed a finite superconducting sample hosts corner Majorana zero modes. We study the behavior of the critical temperature in response to external in-plane magnetic fields. We find an enhancement to the critical temperature that depends on the direction of the magnetic field, which can be directly verified experimentally.

I. INTRODUCTION

The understanding of the role of symmetry and topology on the behavior of materials has been one of the major ongoing developments in the field of condensed-matter physics. Within band theory, it is now well known that distinct phases of topological insulators and superconductors exist [1–4]. A hallmark of these topological phases is the existence of gapless excitations of the surface of a finite sample. For instance, the quantum spin Hall (QSH) state is a two-dimensional (2D) bulk insulating state with two counterpropagating chiral modes that are related by time-reversal symmetry. The QSH state has been observed in mercury telluride quantum wells [5–8] and, more relevant to our work, in monolayer WTe$_2$ at temperatures as high as 100 K [9–15].

Topological superconductors are known to host gapless Majorana modes at the edges, and Majorana zero modes (MZMs) bound at vortex cores. The MZMs are of special interest for their application in quantum computation [16,17]. Despite intensive research and various proposed superconducting materials, unambiguous evidence for topological superconductivity with propagating Majorana modes or MZMs remains elusive. One of the key challenges is that unlike topological insulators, the formation of intrinsic topological superconductivity requires synergy between the normal-state band structure and unconventional pairing symmetry induced by interaction effects.

Recently, the concept of topological insulators and superconductors has been extended to include phases with edges that are gapped except for "higher-order boundaries," that is, a lower-dimensional locus of points on the edge. These new phases have been dubbed higher-order topological insulators and superconductors. Specifically, a nontrivial *n*th-order topology of a *d*-dimensional bulk entails that the gapless parts of the edge are $(d - n)$ dimensional [18–28]. For example, in 2D, a second-order topological superconductor will host Majorana zero modes (MZMs) on the corners of a square sample.

Monolayer WTe$_2$ with odd-parity pairing order has been proposed to be one example of such higher-order topological superconductors [29]. The material is a quantum spin Hall insulator in the normal state, and upon electric gating has been experimentally observed to turn superconducting with a T_c of about 1 K [30,31]. Interestingly, T_c was found to increase in the presence of small in-plane magnetic fields, lending support to possible odd-parity pairing symmetry. Theoretically, in Ref. [29], the authors assumed a next-nearest-neighbor attractive interaction between the electrons and showed that it leads to *p*-wave pairing symmetry. However, the microscopic origin of the attractive interaction remains to be elucidated. Given the small electron density at which superconductivity is observed, in Ref. [32], it was proposed that through virtual interband excitonic processes, the repulsive interactions between electrons can give rise to a *p*-wave pairing instability. However, these results were based on a generic band structure rather than that specific to the monolayer WTe$_2$.

In this work, we argue that a *p*-wave superconducting order parameter in WTe$_2$ follows naturally from the Kohn-Luttinger mechanism of electrons near the Fermi surface. Of course, this mechanism neglects any interband processes, which may be important at low densities, and in this sense is complementary to the pairing mechanism studied in Refs. [32,33]. Kohn and Luttinger first showed that an isotropic electron gas in 3D will develop a superconducting instability for channels with large angular momentum under the effects of screened Coulomb interactions [34–40]. This effect was understood as a consequence of Friedel oscillations [41] that modifies the screened Coulomb interaction, where electrons can take advantage of the attractive portions of the oscillatory potential to form a pair. Kohn-Luttinger-type superconductivity has been recently studied for different lattice systems with short-range interactions [40,42–62]. Even if lattice systems do not have pairing channels with arbitrarily large angular momenta, with proper geometry of the Fermi surface, superconductivity with unconventional pairing symmetry can still emerge out of repulsive interactions.

We model the screened Coulomb interaction between electrons by an on-site repulsive interaction U_0 and study the resulting pairing instability. At the tree level, Cooper pairs

with a nonzero amplitude of being on the same site will experience repulsion of the order of U_0 and cannot form. On the other hand, pairing channels with zero on-site components by construction, which we focus on in this work, do not experience repulsion and have a vanishing tree-level contribution. The fate of these channels can only be determined by renormalizing the interaction vertex to second order in U_0.

Compared with previous works [40,42–62] on the Kohn-Luttinger superconductivity for lattice systems, an important aspect of monolayer WTe$_2$ is the spin-orbit coupling, in which spin singlet and spin triplet are, in general, mixed. As it turned out, despite the existence of spin-orbit coupling in WTe$_2$ [63–67], a spin axis is still conserved [65,68] and there is an approximate residual U(1) spin-rotation symmetry. To their advantage, odd-parity electron pairs with their spin aligned in this direction necessarily have no on-site components due to the Pauli exclusion principle and evade the on-site repulsive interaction U_0, while all other pairing channels have on-site components. We focus on these equal-spin channels and find that when renormalizing the interaction vertex at one-loop order, they lead to the odd-parity pairing instability of WTe$_2$.

Inspired by experimental observations of enhanced T_c by an in-plane magnetic field, we investigate this effect using Landau-Ginzburg free energy. This was also studied in Refs. [32,33]. However, in this work, we make sure that the term added to the free energy respects the U(1) spin-rotational symmetry that is present even when spin-orbit coupling is taken into account. Furthermore, we also take into account that the direction of the spin axis and the direction perpendicular to the plane are not parallel to each other. We find an enhancement to T_c that depends on the direction of the in-plane field. A magnetic field in the **b** direction yields higher enhancement to T_c than a field in the **a** direction of the same magnitude. The reason for this direction dependence is that the spin axis defined by spin-orbit coupling is not perpendicular to the plane of the sample, whereas the results of Refs. [32,33] also show an enhancement to T_c with a small magnetic field; the details of how the enhancement depends on the direction of the field are different from what we find, which can be directly tested experimentally.

With the odd-parity (p-wave) order parameter, monolayer WTe$_2$ hosts two time-reversal Kramer's partners MZMs at the same corner. This situation is very similar to the one studied in Ref. [69] of a heterostructure between a d-wave high-T_c superconductor and a quantum spin-Hall insulator. There, a protocol was developed to braid the two MZMs using an in-plane magnetic field. Unfortunately, we show that this protocol cannot be used in the case of WTe$_2$, since the p-wave pairing order condenses spin and breaks the U(1) spin-rotational symmetry.

The rest of this paper is organized as follows. In Sec. II, we introduce the lattice model for WTe$_2$ in the presence of an on-site repulsive interaction. In Sec. III, we study the pairing gap equation with interactions up to one-loop accuracy, both in real and momentum space. In Sec. IV, we discuss the effects of an in-plane magnetic field in the sample through the formalism of a Ginzburg-Landau theory.
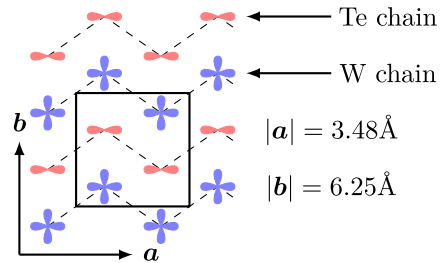

FIG. 1. Monolayer WTe$_2$ unit cell. Depicted are the two W atoms and two Te atoms relevant to the low-energy theory. Each W atom has a d orbital, and each Te atom has a p orbital.

II. NORMAL STATE OF MONOLAYER WTe$_2$

The monolayer WTe$_2$ unit cell has two W atoms and two Te atoms that are relevant to the low-energy theory [65,70]. The lattice consists of W chains and Te chains in an alternating fashion are shown in Fig. 1. The chains are parallel to the **a** direction and stacked along the **b** direction with **b** $\perp$ **a**. Each W atom has a d-wave orbital, while each Te atom has a p-wave orbital. The four orbitals per unit cell are labeled by two pseudospin degrees of freedom, l and σ, where $l_z = \pm 1$ specifies whether it is a W or a Te orbital, and $\sigma_z = \pm 1$ distinguishes their corresponding sublattice. Each orbital can be occupied by either a spin-up or a spin-down electron with $s_z = \pm 1/2$.

The material has an inversion symmetry around the center of the unit cell,

$$\mathcal{I} = \sigma_x l_z. \tag{1}$$

Time-reversal symmetry, $\mathcal{T} = i s_y K$, is also present, with K being the complex conjugate operation. Additionally, the system has a nonsymmorphic glide mirror symmetry $\mathcal{M}_x(\boldsymbol{k}) = s_x[\sigma_0(1 + e^{ik_x}) + \sigma_z(1 - e^{ik_x})]l_z/2$ that is a combination of reflection $\boldsymbol{x} \to -\boldsymbol{x}$ and a half lattice translation in the same direction. Combining inversion and mirror glide gives a screw symmetry $\mathcal{C}_{2x}(\boldsymbol{k}) = \mathcal{M}_x(\boldsymbol{k})\mathcal{I} = s_x[\sigma_x(1 + e^{ik_x}) + i\sigma_y(1 - e^{ik_x})]/2$. This screw symmetry is, in effect, a π rotation about the **a** direction and a half lattice translation along the same direction.

Spin-orbit coupling in WTe$_2$ is significant [63], breaking the SU(2) spin-rotation symmetry. However, it was shown [65] that to leading order in $\boldsymbol{k}$, the system still has a residual spin axis and a U(1) spin-rotation symmetry. We denote this spin axis as $\boldsymbol{z}$, and the spin-orbit coupling can be written as

$$H_{\text{so}} = V_{\text{so}}\, s_z \sigma_z l_y. \tag{2}$$

This z direction is not necessarily perpendicular to the plane of the monolayer WTe$_2$, which we henceforth refer to as the **c** direction. Experimental measurements of the spin axis in Ref. [68] show that the angle between the z and c directions is $\phi_{\text{so}} = 40° \pm 2°$. It is straightforward to check that such a spin-orbit-coupling term is consistent with time-reversal, inversion, and screw symmetries [65] mentioned above. Following this, we exclude additional spin-orbit-coupling terms that further break the U(1) spin-rotation symmetry. In what follows, we
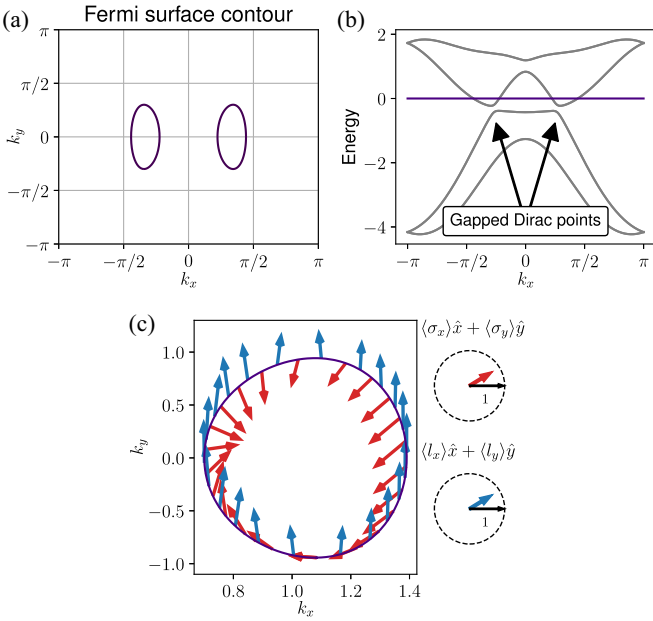
FIG. 2. Spectrum of monolayer WTe$_2$ using the tight-binding model in Ref. [65]. (a) The two Fermi surfaces. (b) The gapped Dirac points. (c) The expectation values of $\boldsymbol{\sigma}$ and $\boldsymbol{l}$ on the Fermi surface. We see that both $|\langle\boldsymbol{\sigma}\rangle|$ and $|\langle\boldsymbol{l}\rangle|$ are approximately one, indicating an approximate absence of entanglement in σ and l. Further, there is a winding in $\langle\boldsymbol{\sigma}\rangle$, while $\langle\boldsymbol{l}\rangle$ does not vary appreciably.

will simply refer to the z component of the electronic spin as "spin."

To obtain an effective model for the low-energy fermions, we start from the tight-binding model fitted from density functional theory in Ref. [65],

$$
\mathcal{H}_0(\boldsymbol{k}) = s_0 \otimes
\begin{bmatrix}
\varepsilon_d & 0 & t_d^{AB} g e^{ik_y} & t_0^{AB} f \\
0 & \varepsilon_p & -t_0^{AB} f & t_p^{AB} g \\
t_d^{AB} g^* e^{-ik_y} & -t_0^{AB} f^* & \varepsilon_d & 0 \\
t_0^{AB} f^* & t_p^{AB} g^* & 0 & \varepsilon_p
\end{bmatrix}
$$
$$
+ V_{\mathrm{so}} s_z \sigma_z l_y - \mu, \tag{3}
$$

where the 2×2 subblocks represent sublattice σ degrees of freedom. The dispersion is specified by

$$
\varepsilon_{d/p}(k_x) = \mu_{d/p} + 2[t_{d/p}\cos(k_x) + t'_{d/p}\cos(2k_x)],
$$
$$
g(k_x) = (1 + e^{-ik_x}), \quad f(k_x) = (1 - e^{-ik_x}), \tag{4}
$$

and

$$
\begin{aligned}
&\mu_d = 0.4935, \ \mu_p = -1.3265, \\
&t_d = -0.28, \ t'_d = 0.075, \\
&t_p = 0.93, \ t'_p = 0.075, \\
&t_d^{AB} = 0.52, \ t_p^{AB} = 0.40, \ t_0^{AB} = 1.02, \\
&V_{\mathrm{so}} = 0.115, \ \mu = 0.5.
\end{aligned} \tag{5}
$$

We plot the Fermi-surface contours in Fig. 2(a). There are two Fermi-surface pockets each enclosing a gapped Dirac point, as shown in Fig. 2(b). The gap is of the order of V_{so}. Moreover, in Fig. 2(c), we plot the expectation values

$\langle\boldsymbol{\sigma}\rangle = (\langle\sigma_x\rangle, \langle\sigma_y\rangle, \langle\sigma_z\rangle)$ and $\langle\boldsymbol{l}\rangle = (\langle l_x\rangle, \langle l_y\rangle, \langle l_z\rangle)$ for the Fermi surface in the $+k_x$ half plane.

We see in Fig. 2(c) that to a good approximation, Bloch states on the Fermi surface are direct product states between σ and l degrees of freedom. Indeed, we see that the lengths $\langle\boldsymbol{\sigma}\rangle$ and $\langle\boldsymbol{l}\rangle$ are almost unity, indicating pure states in each sector. Moreover, we see that $\langle\boldsymbol{l}\rangle$ is approximately a constant pointing in the $+y$ direction, while $\langle\boldsymbol{\sigma}\rangle$ approximately lies in the xy plane and winds once around the Fermi surface. This result can be understood from the symmetry

$$
\mathcal{C}_{2x} = s_x[\sigma_x(1 + e^{ik_x}) + i\sigma_y(1 - e^{ik_x})]/2, \tag{6}
$$

for all states with $k_x = 0$, which, in the absence of spin-orbit coupling, requires the Bloch states to be polarized in σ. For small spin-orbit coupling and for small pockets near $k_y = 0$, the Bloch states are thus nearly free of entanglement in the σ and l sectors. By expanding around the Dirac points and treating other terms in the Hamiltonian as perturbations, one obtains the winding in $\langle\boldsymbol{\sigma}\rangle$ and polarization in $\langle\boldsymbol{l}\rangle$.

With this important simplification, we write the Hamiltonian near the Dirac points as

$$
\mathcal{H}_n^{\pm}(\delta\boldsymbol{k}) = -(\pm v_x \delta k_x \tilde{\sigma}_x^{\pm} + v_y \delta k_y \tilde{\sigma}_y^{\pm} \pm V_{\mathrm{so}} s_z \sigma_z) - \mu, \tag{7}
$$

where $H_n^{\pm}(\delta\boldsymbol{k})$ is the projected Hamiltonian with $l_y = \pm$ for the Fermi surfaces on the $\pm x$ half plane. The Pauli operators $\tilde{\sigma}_\alpha^{\pm}$ are defined in the following way:

$$
\tilde{\sigma}_r^{\pm} = e^{\pm iK\sigma_z/2} \sigma_r e^{\mp iK\sigma_z/2}, \tag{8}
$$

where $r = x, y$, and K is the magnitude of the position of the center of any of the Fermi surfaces. This definition is necessary in order to maintain the screw symmetry of the model. See Appendix A for more details.

While this Hamiltonian does not match the exact shape of the Fermi surfaces or the exact pseudospin texture, it does represent the correct winding and polarization in the σ and l sectors and respects the symmetry. We expect this to be sufficient to capture the symmetry of the superconducting leading instability.

Finally, we model the electron-electron repulsion using a simple on-site interaction U_0. Importantly, the term "on-site" here means that the electron density operators are not only taken at the same unit cell coordinate $\boldsymbol{R}$, but also at the same orbital and same sublattice. Of course, in the actual material, there are finite-range elements to the interaction, but we expect them to fall off rapidly as the distance grows. Let $c_{s,\alpha}(\boldsymbol{R})$ be the annihilation operator for a spin s electron at the α orbital inside the unit cell at position $\boldsymbol{R}$. Note that our notation is such that the index $\alpha = \{1, 2, 3, 4\}$ labels both the $\sigma_z = \pm 1$ and $l_z = \pm 1$ components. The on-site repulsive interaction is written as

$$
H_{\mathrm{int}} = U_0 \sum_{\boldsymbol{R},\alpha} c_{\uparrow,\alpha}^\dagger(\boldsymbol{R}) c_{\downarrow,\alpha}^\dagger(\boldsymbol{R}) c_{\downarrow,\alpha}(\boldsymbol{R}) c_{\uparrow,\alpha}(\boldsymbol{R}), \tag{9}
$$

where $U_0 > 0$ is the strength of the interaction and repeated indices are summed over.

III. THE PAIRING PROBLEM

The point group of monolayer WTe$_2$ is C_{2h}, containing E (the identity), $\mathcal{C}_{2x}$, $\mathcal{M}_x$, and $\mathcal{I}$, with $\mathcal{M}_x\mathcal{C}_{2x} = \mathcal{I}$ and

TABLE I. Irreducible representations of WTe$_2$ point group.

	η_E	η_C	$\eta_{\mathcal{M}}$	$\eta_{\mathcal{I}}$
A_g	$+1$	$+1$	$+1$	$+1$
B_g	$+1$	-1	-1	$+1$
A_u	$+1$	$+1$	-1	-1
B_u	$+1$	-1	$+1$	-1

$\mathcal{C}_{2x}^2 = \mathcal{M}_x^2 = \mathcal{I}^2 = E$. This group has four irreducible representations corresponding to the different signs of $\mathcal{C}_{2x}$ and $\mathcal{M}_x$, as shown in Table I.

We consider the pairing vertex $\int d\boldsymbol{k}\, c^\dagger(\boldsymbol{k})\Delta(\boldsymbol{k})c^\dagger(-\boldsymbol{k})$, in which $\Delta(\boldsymbol{k})$ is a matrix in σ, s, and l. All pairing wave functions must satisfy the Pauli exclusion principle,

$$\Delta^T(-\boldsymbol{k}) = -\Delta(\boldsymbol{k}). \tag{10}$$

Solutions of the gap equation can be characterized depending on how they transform under $\mathcal{C}_{2x}$ and $\mathcal{M}_x$,

$$\mathcal{M}_x : \Delta(\boldsymbol{k}) \to \mathcal{M}_x(\boldsymbol{k})\Delta(\mathcal{M}_x\boldsymbol{k})\mathcal{M}_x^T(-\boldsymbol{k}) = \eta_{\mathcal{M}}\Delta(\boldsymbol{k}), \tag{11}$$

$$\mathcal{C}_{2x} : \Delta(\boldsymbol{k}) \to \mathcal{C}_{2x}(\boldsymbol{k})\Delta(\mathcal{C}_x\boldsymbol{k})\mathcal{C}_{2x}^T(-\boldsymbol{k}) = \eta_{\mathcal{C}}\Delta(\boldsymbol{k}), \tag{12}$$

where $\eta_{\mathcal{M}}$ and $\eta_{\mathcal{C}} \in \{-1, +1\}$. The above equations invoke the form of symmetries at both $\boldsymbol{k}$ and $-\boldsymbol{k}$ because the pairing is between electrons with opposite momenta. Furthermore, we refer to the A_g and B_g representations as the s wave, and the A_u and B_u representations as the p wave.

Before the projection to the vicinity of the Fermi surface, we begin by studying the pairing problem for the full lattice model in real space. Let $\Delta_{\alpha_1\alpha_2}^{s_1 s_2}(\boldsymbol{R}_2 - \boldsymbol{R}_1)$ be the pairing amplitude between an electron at $\boldsymbol{R}_1$, α_1 and another at $\boldsymbol{R}_2$, α_2 with spins s_1 and s_2, respectively. The linearized self-consistent equation for $\Delta_{\alpha_1\alpha_2}^{s_1 s_2}(\boldsymbol{R}_2 - \boldsymbol{R}_1)$ is depicted in Fig. 3, which is

$$\Delta_{\alpha_1\alpha_2}^{s_1 s_2}(\boldsymbol{R}_2 - \boldsymbol{R}_1) = -T \sum_\omega \Gamma^{\alpha_1\alpha_2, \alpha_1'\alpha_2'}(\boldsymbol{R}_1, \boldsymbol{R}_2, \boldsymbol{R}_1', \boldsymbol{R}_2') G_{\alpha_1', \alpha_1''}^{s_1, s_1''}$$

$$\times (i\omega, \boldsymbol{R}_1' - \boldsymbol{R}_1'') G_{\alpha_2', \alpha_2''}^{s_2, s_2''}(-i\omega, \boldsymbol{R}_2' - \boldsymbol{R}_2'')$$

$$\times \Delta_{\alpha_1''\alpha_2''}^{s_1'' s_2''}(\boldsymbol{R}_2'' - \boldsymbol{R}_1''), \tag{13}$$

where, for compactness, repeated indices and spatial coordinates are summed over (for the rest of the paper, it is generally not assumed so). Here, due to the spin-rotation symmetry, the Green's function $G_{\alpha_1', \alpha_1''}^{s_1, s_1''}(\omega_m, \boldsymbol{R}_1' - \boldsymbol{R}_1'')$ is diagonal in the spin sector, but is a matrix in α and the unit cell coordinate $\boldsymbol{R}$. Here, ω_m is a Matsubara frequency, which is summed over.

We note that although, in general, the gap equation is difficult to solve in real space, doing so simplifies the problem for the interaction vertex Γ at the tree level, as we shall see next.
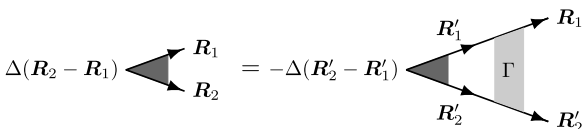

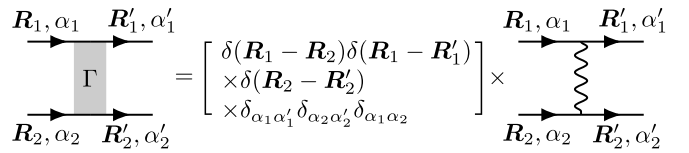
FIG. 3. Linearized gap equation in real space.

FIG. 4. Real-space tree-level interaction vertex.

A. Tree-level pairing interaction

As we show in Fig. 4, at tree level, the interaction vertex function is given by the on-site interaction,

$$\Gamma^{\alpha_1\alpha_2, \alpha_1'\alpha_2'}(\boldsymbol{R}_1, \boldsymbol{R}_2, \boldsymbol{R}_1', \boldsymbol{R}_2') = U_0 \delta(\boldsymbol{R}_1 - \boldsymbol{R}_2)\delta(\boldsymbol{R}_1 - \boldsymbol{R}_1')$$

$$\times \delta(\boldsymbol{R}_2 - \boldsymbol{R}_2')\delta_{\alpha_1\alpha_2}\delta_{\alpha_1\alpha_1'}\delta_{\alpha_2\alpha_2'}$$

$$+ O(U_0^2), \quad U_0 > 0. \tag{14}$$

As a consequence of the repulsive interaction, at leading order in U_0, the right-hand side of Eq. (13) is nonpositive. The key insight here is that to evade the strong on-site repulsion at tree level, we expect the leading instability to be towards a pairing order that has vanishing on-site component *by symmetry*; any other eigenfunction of the kernel of Eq. (13), in general, has an on-site component, which invokes a negative contribution at leading order to the right-hand side of Eq. (13).

Naturally, equal-spin pairing orders (with Cooper pairs of electrons with the same s_z) have zero on-site components by symmetry due to the Pauli exclusion principle. From this argument, we conclude that the leading instability is toward equal-spin pairing. Such a pairing order experiences no repulsion at tree level and, as we shall see, attractive pairing interactions come from $O(U_0^2)$ order. Indeed, we have verified, by using a momentum-space approach near the Fermi surface, that all interspin pairing orders experience a repulsive interaction at tree level. This is reminiscent of the fact that short-range repulsion promotes finite-angular-momentum pairing in the continuum [35].

For a multiorbital system, in principle, it is possible to have equal-spin and even-parity pairing order, e.g., by considering pairing between a W orbital and a Te orbital. However, from energetic considerations of the Cooper instability, it is sensible to limit to pairing between electrons that are inversion partners. In this case, from Fermi statistics, the equal-spin pairing function is necessarily odd in parity, i.e., p wave. We will see this explicitly by going to $O(U_0^2)$ terms in the interaction vertex.

B. Renormalized interactions

The effective attraction for the equal-spin pairing channels comes from U_0^2 order in the interaction vertex. Without loss of generality, we focus only on the spin-$\uparrow\uparrow$ channel. As neither the Green's function nor the density-density interaction flips the spin, we suppress the spin indices throughout. The pairing vertex for the spin-$\downarrow\downarrow$ channel is related by time-reversal symmetry. In Fig. 5, we show the diagrams involved in the vertex calculation up to second-order terms. As is typical for Kohn-Luttinger-type pairing with local interactions, it is straightforward to see that the first three $O(U_0^2)$ diagrams in Fig. 5(b) cancel each other. Evaluation of the last
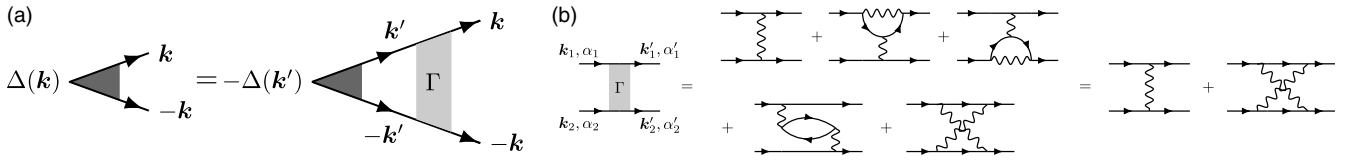
FIG. 5. (a) Linearized gap equation in momentum space. (b) Equal-spin interaction vertex to second order. $\alpha_1, \alpha_2, \alpha_1',$ and, α_2' are combined indices for σ and l.

diagrams leads to

$$\Gamma^{\alpha_1, \alpha_2, \alpha_1', \alpha_2'}(\boldsymbol{k}_1, \boldsymbol{k}_2, \boldsymbol{k}_1', \boldsymbol{k}_2')$$

$$= \left[U_0 \delta_{\alpha_1 \alpha_1'} \delta_{\alpha_2, \alpha_2'} \delta_{\alpha_1, \alpha_2} + U_0^2 \delta_{\alpha_1 \alpha_2'} \delta_{\alpha_2 \alpha_1'} \Pi^{\alpha_1 \alpha_2}(\boldsymbol{k}_1 - \boldsymbol{k}_2') \right]$$

$$\times \, \delta(\boldsymbol{k}_1 + \boldsymbol{k}_2 - \boldsymbol{k}_1' - \boldsymbol{k}_2'), \tag{15}$$

with $\Pi^{\alpha_2 \alpha_1}(\boldsymbol{q})$ being the particle-hole bubble,

$$\Pi^{\alpha_2 \alpha_1}(\boldsymbol{q}) = -\int \frac{d\omega d\boldsymbol{p}}{(2\pi)^3} G^{\alpha_2 \alpha_1}(i\omega, \boldsymbol{p}) G^{\alpha_1 \alpha_2}(i\omega, \boldsymbol{p} - \boldsymbol{q}), \tag{16}$$

and $G^{\alpha_1, \alpha_2}(i\omega, \boldsymbol{k})$ is the Green's function.

The dominant contribution to the Green's function relevant to pairing comes near the Fermi surface. As a good approximation, we take

$$G(i\omega, \boldsymbol{k}) = \frac{|\psi(\boldsymbol{k})\rangle \langle \psi(\boldsymbol{k})|}{i\omega - \varepsilon(\boldsymbol{k})}, \tag{17}$$

where $|\psi(\boldsymbol{k})\rangle$ is the Bloch state of the band that crosses the Fermi level at $\boldsymbol{k}$, and $\epsilon(\boldsymbol{k})$ is its energy. Note that because we are only considering one spin species, there is only one $|\psi(\boldsymbol{k})\rangle$ at each point on the Fermi surface.

The projected gap equation onto the Fermi surface reads

$$\tilde{\Delta}(\boldsymbol{k}) = -\int \frac{d\boldsymbol{k}'}{(2\pi)^2} \tilde{\Gamma}(\boldsymbol{k}, \boldsymbol{k}') \tilde{\Delta}(\boldsymbol{k}') \frac{\tanh(\varepsilon(\boldsymbol{k}')/2T_c)}{2\varepsilon(\boldsymbol{k}')}, \tag{18}$$

where the projected interaction vertex $\tilde{\Gamma}(\boldsymbol{k}', \boldsymbol{k}) = \langle \Psi(\boldsymbol{k}')|\Gamma|\Psi(\boldsymbol{k})\rangle$, with $|\Psi(\boldsymbol{k})\rangle = |\psi(\boldsymbol{k})\rangle \otimes |\psi(-\boldsymbol{k})\rangle$, is given by

$$\tilde{\Gamma}(\boldsymbol{k}', \boldsymbol{k}) = U_0 \sum_{\alpha} \psi_\alpha^*(\boldsymbol{k}') \psi_\alpha^*(-\boldsymbol{k}') \psi_\alpha(\boldsymbol{k}) \psi_\alpha(-\boldsymbol{k})$$

$$+ U_0^2 \sum_{\alpha_2 \alpha_1} \Pi^{\alpha_2 \alpha_1}(\boldsymbol{k} + \boldsymbol{k}') \psi_{\alpha_2}^*(\boldsymbol{k}') \psi_{\alpha_1}^*(-\boldsymbol{k}') \tag{19}$$

$$\times \, \psi_{\alpha_1}(\boldsymbol{k}) \psi_{\alpha_2}(-\boldsymbol{k}),$$

and the pairing gap

$$\tilde{\Delta}(\boldsymbol{k}) = \sum_{\alpha\beta} \psi_\alpha^*(\boldsymbol{k}) \psi_\beta^*(-\boldsymbol{k}) \Delta_{\alpha\beta}(\boldsymbol{k}) \tag{20}$$

is the projection of $\Delta(\boldsymbol{k})$ onto the Fermi surface. Plugging Eq. (10) into Eq. (20), we obtain that by Fermi statistics, $\tilde{\Delta}(\boldsymbol{k}) = -\tilde{\Delta}(-\boldsymbol{k})$. Since the Fermi-surface states are nondegenerate for each spin, inversion simply takes $\tilde{\Delta}(\boldsymbol{k})$ to $\tilde{\Delta}(-\boldsymbol{k})$, and the equal-spin pairing gap corresponds to a p-wave order.

The integral over energy in Eq. (18) gives the usual $\ln(\Lambda/T_c)$, where Λ is the energy cutoff. What is left is the angular integral over the oval Fermi surfaces. For the p-wave solution, we can rewrite the self-consistent equation as

$$\Delta(\theta) = -\int d\theta' \, \Gamma(\theta, \theta') \nu(\theta') \Delta(\theta') \ln\left(\frac{\Lambda}{T_c}\right), \tag{21}$$

where θ parametrizes the momentum on the Fermi surface, as shown in Fig. 6, $\Delta(\theta) = \Delta(\boldsymbol{k}_\theta)$, and

$$\Gamma(\theta, \theta') = \tilde{\Gamma}(\boldsymbol{k}_\theta, \boldsymbol{k}_{\theta'}) - \tilde{\Gamma}(\boldsymbol{k}_\theta, -\boldsymbol{k}_{\theta'}). \tag{22}$$

We use the density of states, $\nu(\theta)$, for the model in Eq. (7),

$$\nu(\theta) = \frac{1}{(2\pi)^2} \frac{\mu}{v_x^2 \cos^2(\theta) + v_y^2 \sin^2(\theta)}. \tag{23}$$

The pairing gap is an eigenfunction given by

$$\lambda \Delta(\theta) = -\int d\theta' \, \Gamma(\theta, \theta') \nu(\theta') \Delta(\theta'). \tag{24}$$

As usual, the pairing channel with $\lambda > 0$ has a critical temperature,

$$T_c = \Lambda \exp\left(-\frac{1}{\lambda}\right). \tag{25}$$

One feature of $\Gamma(\theta, \theta')$ that is immediately obvious is that the first-order contribution in U_0 is zero. This can be seen from Eq. (19), as terms proportional to U_0 are symmetric under $\boldsymbol{k} \to -\boldsymbol{k}$, and thus cancel out in $\Gamma(\theta, \theta')$; this is precisely what we discussed in the previous section. In the following, we focus on second-order terms for the scattering matrix Γ.

We evaluate $\Gamma(\theta, \theta')$ numerically. In Fig. 7, we show our result for $\tilde{\Gamma}(\boldsymbol{k}_\theta, \boldsymbol{k}_{\theta'})$ and $\tilde{\Gamma}(\boldsymbol{k}_\theta, -\boldsymbol{k}_{\theta'})$, where $\boldsymbol{k}_\theta$ and $\pm\boldsymbol{k}_{\theta'}$ belong to the same/different Fermi surface. The most pertinent feature of the result is that $\Gamma(\boldsymbol{k}_\theta, \boldsymbol{k}_{\theta'}) < \Gamma(\boldsymbol{k}_\theta, -\boldsymbol{k}_{\theta'})$ for all θ and θ'. This lead to $\Gamma(\theta, \theta') < 0$ and to $\lambda > 0$.

We note that our analysis relies on an expansion around the Fermi surface. For small values of μ, the interplay between the conduction and valence bands may become important and, as studied in Refs. [32,33], can lead to odd-parity superconductivity without consideration of the Kohn-Luttinger effects. The Kohn-Luttinger effects that we consider here are, in this
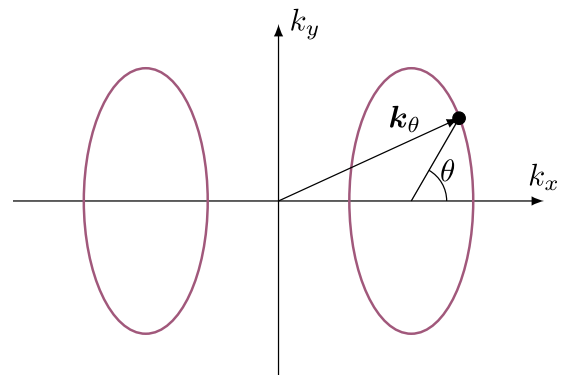

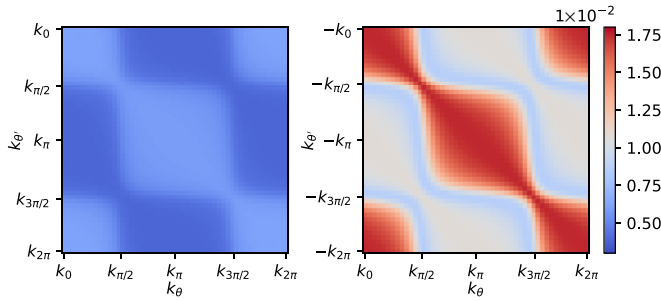FIG. 6. Definition of $\boldsymbol{k}_\theta$ on the Fermi surface.

FIG. 7. Numerical evaluation of the second-order terms of $\tilde{\Gamma}(\boldsymbol{k}_{\theta'}, \boldsymbol{k}_{\theta})$ (left) and $\tilde{\Gamma}(-\boldsymbol{k}_{\theta'}, \boldsymbol{k}_{\theta})$ (right). As discussed in the main text, we see that, in general, $\tilde{\Gamma}(\boldsymbol{k}_{\theta'}, \boldsymbol{k}_{\theta}) < \tilde{\Gamma}(-\boldsymbol{k}_{\theta'}, \boldsymbol{k}_{\theta})$, which is important in obtaining a p-wave superconducting channel with positive λ. $\mu = 0.3$, $v_x = 1$, $v_y = 1/3$, $V_{sc} = 0.1$.

sense, complementary to the results there and further elucidate the exact form of the odd-parity pairing order.

C. Origin of effective attraction

The details of Fig. 7 are complicated by the pseudospin texture on the Fermi surfaces. However, the important features that make solutions with positive λ possible are easily understood from the polarization bubble $\tilde{\Gamma}(\boldsymbol{k}, \boldsymbol{k}')$, which is

$$\Pi(\boldsymbol{q}) = \int \frac{d\boldsymbol{p}}{(2\pi)^2} \frac{f(\varepsilon(\boldsymbol{p})) - f(\varepsilon(\boldsymbol{p} - \boldsymbol{q}))}{\varepsilon(\boldsymbol{p}) - \varepsilon(\boldsymbol{p} - \boldsymbol{q})}, \quad (26)$$

where $\boldsymbol{q} = \boldsymbol{k} + \boldsymbol{k}'$, and $f(\varepsilon)$ is the Fermi-Dirac function. The integrand of $\Pi(\boldsymbol{q})$ is peaked when $\boldsymbol{p}$ and $\boldsymbol{p} - \boldsymbol{q}$ are both near one of the Fermi surfaces. For small $\boldsymbol{q}$, the dominant contribution comes from when both $\boldsymbol{p}$ and $\boldsymbol{p} - \boldsymbol{q}$ are on one of the two Fermi pockets, while for $\boldsymbol{q}$ larger than the size of the Fermi pocket, the dominant contribution can only come from when $\boldsymbol{p}$ is on one Fermi pocket and $\boldsymbol{p} - \boldsymbol{q}$ is on another. We hence have, e.g., $\Pi(0) = 2\Pi(2\boldsymbol{K})$, where $2\boldsymbol{K}$ is the separation of the two Dirac points. This relation also extends to that between $\Pi(\boldsymbol{q}) = 2\Pi(2\boldsymbol{K} + \boldsymbol{q})$, where $\boldsymbol{q}$ is smaller than the size of a Fermi pocket. For this reason, the projected interaction vertices satisfy $\tilde{\Gamma}(\boldsymbol{k}_{\theta'}, \boldsymbol{k}_{\theta}) < \tilde{\Gamma}(-\boldsymbol{k}_{\theta'}, \boldsymbol{k}_{\theta})$, as found in Fig. 7.

Analytically, $\Pi(0)$ is simply the density of states $\nu(\mu)$ at the Fermi level. For $\mu \gg V_{so}$, the density of states is given by a Dirac-like spectrum with a linear density of states, and thus $\Pi(0) \propto \mu$. In this situation, the coupling constant in Eq. (25) satisfies $\lambda \propto \mu$. Using this, and our discussion above, our result indicates an exponential increase in the critical temperature with increasing chemical potential at large dopings. At small dopings, when $\mu \gtrsim V_{so}$, $\Pi(0) = \nu(\mu)$ tends to a constant. However, as we discuss below, T_c will be exponentially suppressed by another mechanism. Experimentally, a sharp increase in superconductivity with doping has been observed in Refs. [30,31], even at very small doping. Therefore, an additional pairing mechanism such as that from interband effects [32,33] is likely required to explain the experimental data.

From Eq. (19), another contribution to $\tilde{\Gamma}(\boldsymbol{k}, \boldsymbol{k}')$ comes from the matrix elements due to the pseudospin texture of the Fermi surfaces. An essential ingredient to achieving the effective attraction between the Cooper pairs is the Dirac dispersion,

which provides an in-plane component to the spinors on the Fermi surface. To show this, it is helpful to consider a hypothetical situation without the Dirac dispersion, in which the spinors are completely determined by the spin-orbit coupling. In this case, we can take the spinors on each Fermi surface as constant. Focusing on the equal-spin states with $+s_z$, the relevant spinors are *polarized* as $\psi(\boldsymbol{k}) = |+s_z, +\sigma_z, +l_y\rangle$ for the Fermi surface at $\boldsymbol{K}$ and $\psi(-\boldsymbol{k}) = |+s_z, -\sigma_z, -l_y\rangle$ for the opposite Fermi surface. One can directly evaluate $\tilde{\Gamma}(\boldsymbol{k}', \boldsymbol{k})$ in Eq. (19) and verify that at both U_0 and U_0^2 orders, it vanishes for any $\boldsymbol{k}$, and $\boldsymbol{k}'$ on either of the two Fermi surfaces. Indeed, the polarized spinors indicate that the leftmost external fermion lines in the Kohn-Luttinger diagram (the last one in Fig. 5) relevant to the pairing process (with opposite momenta) correspond to fermions fully polarized on opposite sublattices (with $\sigma_z = \pm 1$). Since the interaction is on site, which enforces the same sublattice index for all four fermion operators, the scattering amplitudes by both of the wavy lines are zero. By contrast, the presence of the Dirac dispersion ensures the fermions on the Fermi surface (FS) are located coherently on both sublattice sites (in the limit of no spin-orbit coupling, a Bloch state on the FS is an equal superposition between two sublattices), and thus the scattering amplitude is nonzero even for pairing between fermions with opposite sublattice composition. At low dopings, the sublattice texture on the FS is dominated by the spin-orbit coupling and nearly polarized. In this situation, pairing from the Kohn-Luttinger mechanism is indeed exponentially suppressed and, as we mentioned, an additional pairing mechanism, e.g., interband effects, is indeed needed.

Therefore, we conclude that both the Fermi-surface geometry and the underlying Dirac points, even though they are gapped by the spin-orbit interaction, lead to superconductivity due to the Kohn-Luttinger mechanism in WTe$_2$. We note that the same effect was shown to lead to superconducting instabilities in a graphenelike system [42]. Due to the different point-group symmetry, the pairing symmetry there was found to be f wave. As we shall see, another difference is the role of spin-orbit coupling, which is negligible in graphene but not in the present system.

D. Order parameter symmetry representation

Our theory only puts constraints on the projection of the order parameter on the Fermi surfaces. These constraints have already pinned down the order parameter to be a p wave. However, we might still ask if the Kohn-Luttinger mechanism favors A_u representations over B_u representations, or vice versa.

Consider the following $\Delta(\boldsymbol{k})$ making an A_u representation,

$$\Delta_1(\boldsymbol{k}) \propto \sin(k_x) s_0 \sigma_0 l_0. \quad (27)$$

Being a p-wave equal-spin pairing channel, we only need to check if it has a nonzero projection onto the Fermi surface in order to determine if it is a valid order parameter. Using Eq. (20) and the states near the Fermi surface from the simplified Hamiltonian in Eq. (7), $|\psi(\boldsymbol{k})\rangle = (1, \pm i)^T \otimes [\cos(\theta/2), \sin(\theta/2)e^{i\phi}]^T/2$, and $|\psi(-\boldsymbol{k})\rangle = [1, -(\pm i)]^T \otimes [\sin(\theta/2), \cos(\theta/2)e^{-i\phi}]^T/2$, we find the projection of $\Delta_1(\boldsymbol{k})$

onto the Fermi surface,

$$\tilde{\Delta}_1(\boldsymbol{k}) \propto \sin(k_x) \sum_\alpha \psi_\alpha^*(\boldsymbol{k})\psi_\alpha^*(-\boldsymbol{k})s_0 = \sin(k_x)\sin(\theta)s_0. \quad (28)$$

In the case of zero spin-orbit coupling, we have $\theta = \pi/2$, and as spin-orbit coupling increases, θ decreases.

Meanwhile, B_u representations can also describe an equal-spin p wave with nonzero projection into the Fermi surface. Consider the following example:

$$\Delta_2(\boldsymbol{k}) \propto \sin(k_x)s_z\sigma_0 l_0, \quad (29)$$

which has a projection

$$\tilde{\Delta}_2(\boldsymbol{k}) \propto \sin(k_x)\sin(\theta)s_z. \quad (30)$$

We see that Δ_1 and Δ_2 correspond to the equal and opposite pairing amplitudes among spin-up and spin-down fermions. Due to the additional U(1) spin-rotation symmetry that relates the two, both A_u and B_u representations are equally favored by the Kohn-Luttinger mechanism.

In reality, the U(1) spin-rotation symmetry is weakly broken in the normal state. This symmetry breaking could be the effect of a small momentum-dependent spin-orbit coupling or due to electron interactions. In either case, these effects are expected to remove the degeneracy between Δ_1 and Δ_2. Whether Δ_1 or Δ_2 ends up being the leading instability will depend on the details of the breaking of the U(1) symmetry in the system, which can be calculated either using perturbation theory or by including a $|\Delta_1|^2 - |\Delta_2|^2$ term in the free energy. To the best of our knowledge, the details of the U(1) symmetry have not been explored numerically or experimentally. We hope that our work further motivates exploration in this area.

It is important to note that the superconducting states Δ_1 and Δ_2 would break the U(1) spin-rotation symmetry $e^{i\theta s_z}$. This can be seen by writing

$$\Delta(\boldsymbol{k}) \propto \boldsymbol{d} \cdot \boldsymbol{s}\, is_y, \quad (31)$$

in which the $\boldsymbol{d}$ vector is along the $\hat{y}$ and $\hat{x}$ directions for Δ_1 and Δ_2, respectively, and thus breaking the spin-rotation symmetry in the xy plane.

E. Corner Majorana zero modes

In this section, following the identification in Ref. [29], we demonstrate the existence of Majorana corner modes in WTe$_2$ with the leading pairing instability dictated by the Kohn-Luttinger mechanism. We start with the density functional theory (DFT)-fitted tight-binding model in Ref. [65] and add the pairing terms in Eqs. (27) and (29). In Fig. 8(a), we show the distribution eigenvalues around zero energy. We clearly see four modes that are pinned at zero energy. With time-reversal $\mathcal{T}^2 = -1$, these modes are two Kramers pairs, Majorana zero modes. In Fig. 8(b), we plot the average probability distribution in real space for the Majorana zero modes. One Kramer pair is localized at one corner and the other pair is localized on the opposite corner related by inversion. This is consistent with the results in Ref. [29].

Time-reversal symmetry can be broken by the introduction of a magnetic field,

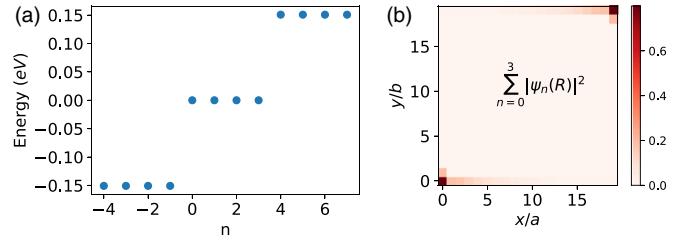$$H_{\text{mag}} = h_x s_x \sigma_0 l_0 + h_y s_y \sigma_0 l_0. \quad (32)$$

FIG. 8. The existence of four Majorana zero modes that are localized on two opposite corners of the sample. Each of the opposite corners has two Majorana zero modes that are Kramer's partners.

With time-reversal symmetry broken, the Majorana zero modes at each corner are no longer Kramer's partners, and they can hybridize and gap each other out. This is also confirmed by our numerical study. This is important to contrast with the Majorana pairs discussed in Ref. [69]. There, the MZMs were obtained from a d-wave superconductor sitting on top of a QSH state. Such heterostructure also results in a Kramer's pair of MZMs at the corners. Using this platform, it is possible to braid the pair of Majoranas by tuning the in-plane magnetic fields. Magnetic fields also break time-reversal symmetry in the heterostructure; however, due to the spin-singlet nature of the pairing order, the system still has a U(1) spin-rotation symmetry in the superconducting state. Thus, in the presence of an in-plane magnetic field, the original time-reversal symmetry $\mathcal{T}$ can be combined with the U(1) symmetry to make a new time-reversal symmetry $\mathcal{T}' = e^{i\pi/2 s_z}\mathcal{T}$ that squares to $+1$. Together with the particle-hole symmetry of the Bogoliubov-de Gennes (BdG) Hamiltonian, this puts the heterostructure in the symmetry class BDI. This composite symmetry ensures that a pair of MZMs of the same chiral eigenvalue is protected, and is one of the prerequisites for braiding the MZMs using in-plane fields. Since the p-wave superconducting order of WTe$_2$ breaks the spin U(1) symmetry, the protocol developed in Ref. [69] cannot be used to braid the MZMs. It remains to be seen what perturbations can be added to manipulate and possibly braid the two MZMs at each corner for the intrinsic p-wave state. Alternatively, one can introduce a d-wave pairing order to monolayer WTe$_2$ via the proximity effect.

IV. EFFECTS OF IN-PLANE EXTERNAL MAGNETIC FIELD

In this section, we study the effect of in-plane external magnetic fields on T_c, using a Ginzburg-Landau theory. In the presence of a magnetic field, the free energy can be written in a form that is explicitly invariant under the U(1) spin rotation,

$$F = [\alpha(T) + \chi B^2](\boldsymbol{d}^* \cdot \boldsymbol{d}) + 2\gamma|d_z|^2$$
$$+ \mu\boldsymbol{B} \cdot (i\boldsymbol{d} \times \boldsymbol{d}^*) + \eta|\boldsymbol{B} \cdot \boldsymbol{d}|^2, \quad (33)$$

where we denote the pairing order parameter by their $\boldsymbol{d}$ vectors defined in Eq. (31), $\alpha = \kappa[T - T_c(\boldsymbol{B} = 0)]$, and $\kappa, \gamma, \mu, \eta, \chi > 0$. Here, μ (not to be confused with the chemical potential) describes the Zeeman effect caused by the magnetic field, and the η term accounts for pair breaking due
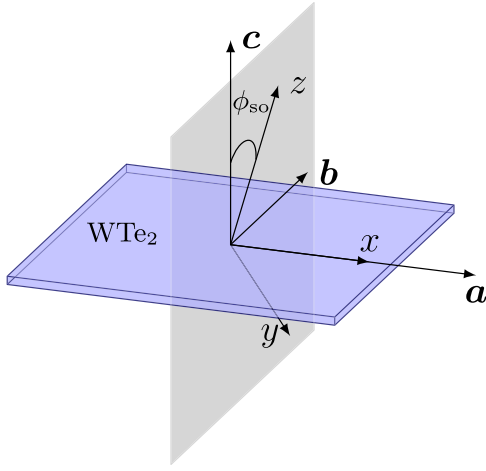
FIG. 9. The a and b directions are the lattice vectors for WTe$_2$, and the c direction is perpendicular to the WTe$_2$ plane. The z direction is the direction of the spin axis picked up by spin-orbit coupling. The x direction is chosen to be parallel to the a direction, and the y direction is perpendicular to the xz plane.

to orbital effects. The γ term is due to the effect of spin-orbit coupling. Indeed, in the absence of spin-orbit coupling, the system has a full SU(2) spin-rotation symmetry and all three d vectors are equally favored by symmetry. We take $\gamma > 0$ such that with no magnetic field, we have the equal-spin channels d_x and d_y being the leading instabilities of the system, as predicted by our Kohn-Luttinger analysis.

Note that the z direction is not perpendicular to the sample plane; rather, it is the direction of spin polarization due to spin-orbit coupling [68]. Thus, in the following, it is important to distinguish between two different coordinate systems. The a, b, c-coordinate system is such that the c direction is perpendicular to the plane of the sample, and the a and b directions are as defined in Fig. 1. On the other hand, the x, y, z-coordinate system is such that $x \parallel a$, while the z direction is in the cb plane at an angle ϕ_{so} with the c direction. See Fig. 9 for an illustration.

We separately study the effect of in-plane magnetic fields along the a and b directions. For $\boldsymbol{B} = B_a\boldsymbol{a}$, the free energy reduces to

$$F = \left[\alpha(T) + \chi B_a^2\right](\boldsymbol{d}^* \cdot \boldsymbol{d}) + 2\gamma|d_z|^2 \\ + \mu B_a i[d_y d_z^* - d_z d_y^*] + \eta|B_a d_x|^2. \quad (34)$$

In this case, the x component of the order parameter does not mix with the other two, and setting $d_x = 0$ always results in a higher critical temperature. Solving the eigenvalue problem for the y and z components gives a critical temperature,

$$T_c(B_a) = T_c(0) - \chi B_a^2 - \gamma + \sqrt{\gamma^2 + \mu^2 B_a^2}. \quad (35)$$

Looking at the behavior near $B_a = 0$ we have $T_c(B_a) = T_c(0) - (\chi - \mu^2/2\gamma)B_a^2$. For $\gamma < \mu^2/2\chi$, small fields enhance the critical temperature. However, for $\gamma > \mu^2/2\chi$, any field is detrimental to superconductivity. We plot both scenarios in Fig. 10 (shown as orange curves).
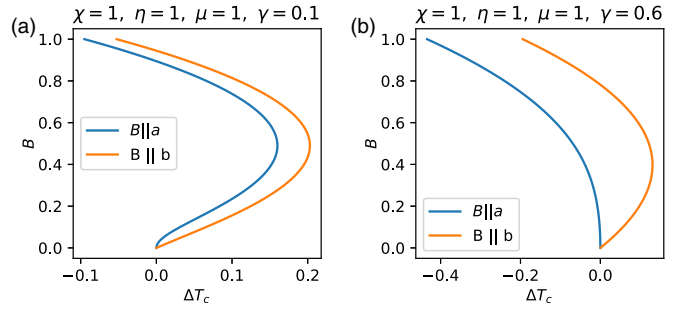

FIG. 10. The dependence of the critical temperature on in-plane magnetic fields, and the strength of the spin-orbit coupling γ. For $\gamma < \mu^2/2\chi$, magnetic fields in the a and b directions cause an enhancement to T_c, with the b-field direction causing bigger enhancement. However, for $\gamma > \mu^2/2\chi$, magnetic fields in the a direction always cause T_c to decrease, while we still see enhancement for fields in the b direction.

Next we consider $\boldsymbol{B} = B_b\boldsymbol{b}$, for which the free energy can be written as

$$F = \left[\alpha(T) + \chi B_b^2\right](\boldsymbol{d} \cdot \boldsymbol{d}^*) + 2\gamma|d_z|^2 \\ + \mu B_b[d_c d_a^* - d_a d_c^*] + \eta|B_b d_b|^2. \quad (36)$$

Unlike the previous case, because of the misalignment between c and z, all components of $\boldsymbol{d}$ are mixed and the behavior of the system depends on ϕ_{so}. For $\phi_{so} = 0$, we have a situation very similar to that when $\boldsymbol{B} = B_a\boldsymbol{a}$, and the critical temperature reduces to Eq. (35). The other limiting case is when $\phi_{so} = 90°$, such that $\hat{z} = \boldsymbol{b}$. In this case, the z component of the order parameter decouples from the other components. The critical temperature, in this case, is

$$T_c(B) = T_c(0) - \chi B^2 + \mu B. \quad (37)$$

When $\phi_{so} = 90°$, the critical temperature increases linearly with the magnetic field for small fields. This is a bigger enhancement to T_c than what we get when $B \parallel a$. Additionally, the enhancement does not depend on how big or small γ is. Real WTe$_2$, however, has $\phi_{so} \approx 40°$. We thus expect the enhancement of the critical temperature with small fields to be somewhere between the two limiting cases.

For the general case, when $\boldsymbol{B} \parallel \boldsymbol{b}$, we write

$$F = \boldsymbol{d}^\dagger[(\alpha + \chi B^2)\mathbb{1} + M]\boldsymbol{d}, \quad (38)$$

with

$$M = \begin{bmatrix} 0 & 0 & i\mu B \\ 0 & \eta B^2 + 2\gamma\sin^2(\phi_{so}) & \gamma\sin(2\phi_{so}) \\ -i\mu B & \gamma\sin(2\phi_{so}) & 2\gamma\cos^2(\phi_{so}) \end{bmatrix}. \quad (39)$$

The problem of finding the T_c reduces to the problem of finding the smallest eigenvalue of M. The characteristic equation $\det(M - \lambda\mathbb{1}) = 0$ is cubic and does not have an easy solution. In Fig. 10, we show the numerical solution to the characteristic equation for $\phi = 40°$. We compare the enhancement to T_c for when $\boldsymbol{B} \parallel \boldsymbol{a}$ and for when $\boldsymbol{B} \parallel \boldsymbol{b}$. Figure 10 clearly shows that $\boldsymbol{B} \parallel \boldsymbol{b}$ yields a bigger enhancement to T_c than $\boldsymbol{B} \parallel \boldsymbol{a}$. In fact,

when $\gamma > \mu^2/2\chi$, Fig. 10(b) shows that we only get enhancement when $\boldsymbol{B} \parallel \boldsymbol{b}$ and not when $\boldsymbol{B} \parallel \boldsymbol{a}$. This is the key finding of our work. The field dependence of T_c has been measured for monolayer WTe$_2$ with similar behaviors observed [71]. It would thus be interesting to examine the dependence of T_c on the direction of the in-plane Zeeman field.

The same problem was studied in Ref. [32], and we point out two ways in which our results differ. First, here we make sure that the spin-orbit-coupling term included in the free energy respects the U(1) spin-rotation symmetry that the normal state enjoys. On the other hand, the authors of Ref. [32] assumed d_z and d_y are degenerate even though they are not related by any symmetries. Second, we take into account the fact that the spin axis in the z direction is not parallel to the c direction. These considerations lead to qualitatively different results. For example, for $\gamma > 0$, the results in Ref. [32] indicate that $\boldsymbol{B} \parallel \boldsymbol{a}$ will not enhance T_c, whereas our result shows that for a sufficiently small spin-orbit coupling, we get T_c enhancement. Furthermore, for $\boldsymbol{B} \parallel \boldsymbol{b}$, the results in Ref. [32] indicate that for a sufficiently large spin-orbit coupling, there is no enhancement to T_c, while our results show that a small field will always lead to an enhancement in T_c, regardless of the value of γ.

V. DISCUSSION

In this work, we studied the superconducting ground state of monolayer WTe$_2$ from on-site repulsive interactions. By constructing an effective model for the Fermi surfaces of WTe$_2$, we show that the leading instability of the system is an equal-spin p-wave channel. This suggests that WTe$_2$ is a second-order topological superconductor with a pair of Majorana zero modes on the corners of a finite sample.

We also studied the effect of an external magnetic field on superconducting monolayer WTe$_2$. Using a Ginzburg-Landau theory, we study the effect of in-plane magnetic fields on T_c. We find an enhancement to T_c at small field strengths. Interestingly, this enhancement is dependent on the direction of the in-plane field. In particular, a field in the $\boldsymbol{b}$ direction yields a bigger enhancement as compared to a field of the same strength but oriented in the $\boldsymbol{a}$ direction. This discrepancy can be used as an experimental tool to confirm the nature of the order parameter in WTe$_2$.

APPENDIX A: SCREW SYMMETRY C_{2x} IN THE SIMPLIFIED HAMILTONIAN

Special care is needed when writing the simplified Hamiltonian in Eq. (7) in order to make sure it respects all symmetries of WTe$_2$. We rewrite the Hamiltonian here for convenience,

$$\mathcal{H}_n^{\pm}(\delta\boldsymbol{k}) = -(\pm v_x \delta k_x \tilde{\sigma}_x^{\pm} + v_y \delta k_y \tilde{\sigma}_y^{\pm} \pm V_{\mathrm{so}} s_z \sigma_z) - \mu. \quad \text{(A1)}$$

The screw symmetry $\mathcal{C}_{2x}$ maps one Fermi surface to itself, and $(\delta k_x, \delta k_y) \to (\delta k_x, -\delta k_y)$. For the Hamiltonian to be invariant $\tilde{\sigma}_\alpha^{\pm}, \alpha = x, y$ should be defined such that

$$\begin{aligned} \mathcal{C}_{2x}^{\dagger} \tilde{\sigma}_x^{\pm} \mathcal{C}_{2x} &= \tilde{\sigma}_x^{\pm}, \\ \mathcal{C}_{2x}^{\dagger} \tilde{\sigma}_y^{\pm} \mathcal{C}_{2x} &= -\tilde{\sigma}_y^{\pm}. \end{aligned} \quad \text{(A2)}$$

Being a screw symmetry, the matrix representation of $\mathcal{C}_{2x}$ depends on momentum, and we rewrite it in the following form:

$$C_{2x} = s_x (1 + e^{ik_x})[\sigma_x + \sigma_y \tan(k_x/2)]. \quad \text{(A3)}$$

This symmetry is effectively a reflection about the axis $[1, \tan(k_x/2)]$ in the xy plane. This line makes an angle θ with the x axis, such that $\tan(\theta) = \tan(k_x/2)$, or $\theta = k_x/2$. To maintain the symmetry, $\tilde{\sigma}_x$ needs to be parallel to this line and $\tilde{\sigma}_y$ needs to be perpendicular to it.

To maintain the simple form of the Dirac Hamiltonian, we approximate $\mathcal{C}_{2x}$ to be constant on each Fermi surface and evaluated at the centers $\pm K$. It is straightforward to check that the following form for $\tilde{\sigma}_\alpha, \alpha = x, y$, preserves the screw symmetry:

$$\begin{aligned} \tilde{\sigma}_\alpha^{+} &= e^{iK\sigma_z/2} \sigma_\alpha e^{-iK\sigma_z/2}, \\ \tilde{\sigma}_\alpha^{-} &= e^{-iK\sigma_z/2} \sigma_\alpha e^{iK\sigma_z/2}. \end{aligned} \quad \text{(A4)}$$
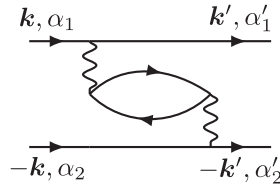
APPENDIX B: CANCELLATION OF FIRST THREE SECOND-ORDER DIAGRAMS

There are four second-order terms contributing to the scattering vertex. However, three of them cancel each other out. Using

$$= U_0 \delta_{\alpha_1 \alpha_1'} \delta_{\alpha_2 \alpha_2'} \delta_{\alpha_1 \alpha_2} \quad \text{(B1)}$$

we can evaluate the following diagrams:

$$= U_0^2 \delta_{\alpha_1 \alpha_1'} \delta_{\alpha_2 \alpha_2'} \int \frac{dp}{(2\pi)^3} G^{\alpha_2 \alpha_1}(p) G^{\alpha_1 \alpha_2}(p - q), \quad \text{(B2)}$$

$$= -2U_0^2 \delta_{\alpha_1\alpha_1'} \delta_{\alpha_2\alpha_2'} \int \frac{dp}{(2\pi)^3} G^{\alpha_2\alpha_1}(p) G^{\alpha_1\alpha_2}(p-q). \tag{B3}$$

Here, $q = k' - k$ and the -2 factor for the bubble diagram is due to the fermionic loop and the spin degeneracy. We thus see that these three diagrams cancel each other out.

---

[1] M. Z. Hasan and C. L. Kane, Rev. Mod. Phys. **82**, 3045 (2010).

[2] X.-L. Qi and S.-C. Zhang, Rev. Mod. Phys. **83**, 1057 (2011).

[3] C.-K. Chiu, J. C. Y. Teo, A. P. Schnyder, and S. Ryu, Rev. Mod. Phys. **88**, 035005 (2016).

[4] E. Witten, La Rivista del Nuovo Cimento **39**, 313 (2016).

[5] B. A. Bernevig, T. L. Hughes, and S.-C. Zhang, Science **314**, 1757 (2006).

[6] M. König, S. Wiedmann, C. Brüne, A. Roth, H. Buhmann, L. W. Molenkamp, X.-L. Qi, and S.-C. Zhang, Science **318**, 766 (2007).

[7] K. C. Nowack, E. M. Spanton, M. Baenninger, M. König, J. R. Kirtley, B. Kalisky, C. Ames, P. Leubner, C. Brüne, H. Buhmann, L. W. Molenkamp, D. Goldhaber-Gordon, and K. A. Moler, Nat. Mater. **12**, 787 (2013).

[8] R. S. Deacon, J. Wiedenmann, E. Bocquillon, F. Domínguez, T. M. Klapwijk, P. Leubner, C. Brüne, E. M. Hankiewicz, S. Tarucha, K. Ishibashi, H. Buhmann, and L. W. Molenkamp, Phys. Rev. X **7**, 021011 (2017).

[9] Y. Shi, J. Kahn, B. Niu, Z. Fei, B. Sun, X. Cai, B. A. Francisco, D. Wu, Z.-X. Shen, X. Xu, D. H. Cobden, and Y.-T. Cui, Sci. Adv. **5**, eaat8799 (2019).

[10] S. Wu, V. Fatemi, Q. D. Gibson, K. Watanabe, T. Taniguchi, R. J. Cava, and P. Jarillo-Herrero, Science **359**, 76 (2018).

[11] S. Tang, C. Zhang, D. Wong, Z. Pedramrazi, H.-Z. Tsai, C. Jia, B. Moritz, M. Claassen, H. Ryu, S. Kahn, J. Jiang, H. Yan, M. Hashimoto, D. Lu, R. G. Moore, C.-C. Hwang, C. Hwang, Z. Hussain, Y. Chen, M. M. Ugeda *et al.*, Nat. Phys. **13**, 683 (2017).

[12] Z. Fei, T. Palomaki, S. Wu, W. Zhao, X. Cai, B. Sun, P. Nguyen, J. Finney, X. Xu, and D. H. Cobden, Nat. Phys. **13**, 677 (2017).

[13] Z.-Y. Jia, Y.-H. Song, X.-B. Li, K. Ran, P. Lu, H.-J. Zheng, X.-Y. Zhu, Z.-Q. Shi, J. Sun, J. Wen, D. Xing, and S.-C. Li, Phys. Rev. B **96**, 041108(R) (2017).

[14] L. Peng, Y. Yuan, G. Li, X. Yang, J.-J. Xian, C.-J. Yi, Y.-G. Shi, and Y.-S. Fu, Nat. Commun. **8**, 659 (2017).

[15] A. Lau, R. Ray, D. Varjas, and A. R. Akhmerov, Phys. Rev. Mater. **3**, 054206 (2019).

[16] S. D. Sarma, M. Freedman, and C. Nayak, npj Quantum Inf. **1**, 15001 (2015).

[17] C. Beenakker, Annu. Rev. Condens. Matter Phys. **4**, 113 (2013).

[18] Z. Yan, Phys. Rev. Lett. **123**, 177001 (2019).

[19] W. A. Benalcazar, B. A. Bernevig, and T. L. Hughes, Science **357**, 61 (2017).

[20] L. Trifunovic and P. W. Brouwer, Phys. Rev. X **9**, 011012 (2019).

[21] M. Geier, L. Trifunovic, M. Hoskam, and P. W. Brouwer, Phys. Rev. B **97**, 205135 (2018).

[22] F. Schindler, A. M. Cook, M. G. Vergniory, Z. Wang, S. S. P. Parkin, B. A. Bernevig, and T. Neupert, Sci. Adv. **4**, eaat0346 (2018).

[23] Y. Wang, M. Lin, and T. L. Hughes, Phys. Rev. B **98**, 165144 (2018).

[24] A. Jahin, A. Tiwari, and Y. Wang, SciPost Phys. **12**, 053 (2022).

[25] A. Tiwari, A. Jahin, and Y. Wang, Phys. Rev. Res. **2**, 043300 (2020).

[26] J. Langbehn, Y. Peng, L. Trifunovic, F. von Oppen, and P. W. Brouwer, Phys. Rev. Lett. **119**, 246401 (2017).

[27] R.-X. Zhang, W. S. Cole, and S. Das Sarma, Phys. Rev. Lett. **122**, 187001 (2019).

[28] H. D. Scammell, J. Ingham, M. Geier, and T. Li, Phys. Rev. B **105**, 195149 (2022).

[29] Y.-T. Hsu, W. S. Cole, R.-X. Zhang, and J. D. Sau, Phys. Rev. Lett. **125**, 097001 (2020).

[30] E. Sajadi, T. Palomaki, Z. Fei, W. Zhao, P. Bement, C. Olsen, S. Luescher, X. Xu, J. A. Folk, and D. H. Cobden, Science **362**, 922 (2018).

[31] V. Fatemi, S. Wu, Y. Cao, L. Bretheau, Q. D. Gibson, K. Watanabe, T. Taniguchi, R. J. Cava, and P. Jarillo-Herrero, Science **362**, 926 (2018).

[32] V. Crépel and L. Fu, Proc. Natl. Acad. Sci. **119**, e2117735119 (2022).

[33] V. Crépel, T. Cea, L. Fu, and F. Guinea, Phys. Rev. B **105**, 094506 (2022).

[34] W. Kohn and J. M. Luttinger, Phys. Rev. Lett. **15**, 524 (1965).

[35] J. M. Luttinger, Phys. Rev. **150**, 202 (1966).

[36] D. Fay and A. Layzer, Phys. Rev. Lett. **20**, 187 (1968).

[37] A. V. Chubukov and M. Y. Kagan, J. Phys.: Condens. Matter **1**, 3135 (1989).

[38] A. V. Chubukov, Phys. Rev. B **48**, 1097 (1993).

[39] A. S. Alexandrov and V. V. Kabanov, Phys. Rev. Lett. **106**, 136403 (2011).

[40] S. Raghu, E. Berg, A. V. Chubukov, and S. A. Kivelson, Phys. Rev. B **85**, 024516 (2012).

[41] J. Friedel, Adv. Phys. **3**, 446 (1954).

[42] R. Nandkishore, R. Thomale, and A. V. Chubukov, Phys. Rev. B **89**, 144501 (2014).

[43] M. L. Kiesel and R. Thomale, Phys. Rev. B **86**, 121105(R) (2012).

[44] M. L. Kiesel, C. Platt, and R. Thomale, Phys. Rev. Lett. **110**, 126405 (2013).

[45] S. Raghu, S. A. Kivelson, and D. J. Scalapino, Phys. Rev. B **81**, 224505 (2010).

[46] O. Vafek, J. M. Murray, and V. Cvetkovic, Phys. Rev. Lett. **112**, 147002 (2014).

[47] J. M. Murray and O. Vafek, Phys. Rev. B **89**, 205119 (2014).

[48] F. Guinea and B. Uchoa, Phys. Rev. B **86**, 134521 (2012).

[49] R. Roldán, E. Cappelluti, and F. Guinea, Phys. Rev. B **88**, 054515 (2013).

[50] S. Wolf, D. Di Sante, T. Schwemmer, R. Thomale, and S. Rachel, Phys. Rev. Lett. **128**, 167002 (2022).

[51] Y.-P. Lin and R. M. Nandkishore, Phys. Rev. B **98**, 214521 (2018).

[52] M. Dürrnagel, J. Beyer, R. Thomale, and T. Schwemmer, Eur. Phys. J. B **95**, 112 (2022).

[53] S. Wolf, T. L. Schmidt, and S. Rachel, Phys. Rev. B **98**, 174515 (2018).

[54] R. M. Nandkishore and S. L. Sondhi, Phys. Rev. X **7**, 041021 (2017).

[55] M. Y. Kagan, V. A. Mitskan, and M. M. Korovushkin, J. Supercond. Novel Magn. **29**, 1043 (2016).

[56] M. Y. Kagan, V. A. Mitskan, and M. M. Korovushkin, J. Low Temp. Phys. **185**, 508 (2016).

[57] M. Y. Kagan, V. A. Mitskan, and M. M. Korovushkin, Phys. Usp. **58**, 733 (2015).

[58] M. Y. Kagan, V. A. Mitskan, and M. M. Korovushkin, Eur. Phys. J. B **88**, 157 (2015).

[59] J. González and T. Stauber, Phys. Rev. Lett. **122**, 026801 (2019).

[60] W. Cho, R. Thomale, S. Raghu, and S. A. Kivelson, Phys. Rev. B **88**, 064505 (2013).

[61] T. Li, M. Geier, J. Ingham, and H. D. Scammell, 2D Mater. **9**, 015031 (2022).

[62] T. Li, J. Ingham, and H. D. Scammell, Phys. Rev. Res. **2**, 043155 (2020).

[63] J. Jiang, F. Tang, X. C. Pan, H. M. Liu, X. H. Niu, Y. X. Wang, D. F. Xu, H. F. Yang, B. P. Xie, F. Q. Song, P. Dudin, T. K. Kim, M. Hoesch, P. K. Das, I. Vobornik, X. G. Wan, and D. L. Feng, Phys. Rev. Lett. **115**, 166601 (2015).

[64] X. Qian, J. Liu, L. Fu, and J. Li, Science **346**, 1344 (2014).

[65] S. Ok, L. Muechler, D. Di Sante, G. Sangiovanni, R. Thomale, and T. Neupert, Phys. Rev. B **99**, 121105(R) (2019).

[66] D.-H. Choe, H.-J. Sung, and K. J. Chang, Phys. Rev. B **93**, 125109 (2016).

[67] F. Zheng, C. Cai, S. Ge, X. Zhang, X. Liu, H. Lu, Y. Zhang, J. Qiu, T. Taniguchi, K. Watanabe, S. Jia, J. Qi, J.-H. Chen, D. Sun, and J. Feng, Adv. Mater. **28**, 4845 (2016).

[68] W. Zhao, E. Runburg, Z. Fei, J. Mutch, P. Malinowski, B. Sun, X. Huang, D. Pesin, Y.-T. Cui, X. Xu, J.-H. Chu, and D. H. Cobden, Phys. Rev. X **11**, 041034 (2021).

[69] M. F. Lapa, M. Cheng, and Y. Wang, SciPost Phys. **11**, 086 (2021).

[70] L. Muechler, A. Alexandradinata, T. Neupert, and R. Car, Phys. Rev. X **6**, 041069 (2016).

[71] T. Asaba, Y. Wang, G. Li, Z. Xiang, C. Tinsman, L. Chen, S. Zhou, S. Zhao, D. Laleyan, Y. Li, Z. Mi, and L. Li, Sci. Rep. **8**, 6520 (2018).